



Nitrogen doped NiFe layered double hydroxide/reduced graphene oxide mesoporous nanosphere as an effective bifunctional electrocatalyst for oxygen reduction and evolution reactions



Tianrong Zhan^{a,*}, Xiaolin Liu^a, SiSi Lu^a, Wanguo Hou^{b,*}

^a Key Laboratory of Sensor Analysis of Tumor Marker (Ministry of Education), State Key Laboratory Base of Eco-chemical Engineering, College of Chemistry and Molecular Engineering, Qingdao University of Science and Technology, Qingdao 266042, China

^b Key Laboratory of Colloid & Interface Chemistry (Ministry of Education), Shandong University, Jinan 250100, China

ARTICLE INFO

Article history:

Received 16 November 2016

Received in revised form

30 December 2016

Accepted 4 January 2017

Available online 4 January 2017

Keywords:

NiFe layered double hydroxide

Reduced graphene oxide

Nitrogen doping

Oxygen evolution reaction

Oxygen reduction reaction

ABSTRACT

It is a crucial and challengeable task to develop non-precious metal catalysts for both oxygen reduction reaction (ORR) and oxygen evolution reaction (OER) in energy storage and conversion systems. Herein, a facile and cost-effective strategy was employed to prepare the mesoporous nitrogen doped NiFe layered double hydroxide/reduced graphene oxide (NiFe-LDH/NrGO) nanospheres via an one-pot solvothermal reaction by using GO, protonated g-C₃N₄ nanosheets (p-CNNS), mixed metal salts and alkali as precursors in presence of surfactant. The doping of p-CNNS resulted in the superior ORR activity compared to pristine NiFe-LDH and NiFe-LDH/rGO. The ORR results demonstrated that the NiFe-LDH/NrGO hybrid involved a perfect 4e mechanism with better durability and methanol tolerance ability than commercial 20% Pt/C catalyst in 0.1 M KOH. NiFe-LDH/NrGO also displayed the excellent OER activity with a close onset overpotential to NiFe-LDH/rGO, but a more negative overpotential and a higher current density at $\eta > 300$ mV in the same alkaline medium. Overall, the outstanding catalytic performance toward both ORR and OER suggested that the NiFe-LDH/NrGO composite can be a new non-precious metal bifunctional catalyst in the related renewable energy fields.

© 2017 Elsevier B.V. All rights reserved.

1. Introduction

Electrochemical oxygen reduction reaction (ORR) in discharging and oxygen evolution reaction (OER) in charging are unambiguously the pivotal electrode processes for many sustainable energy technologies such as metal–air batteries, regenerative fuel cells and water splitting [1–3]. However, both OER and ORR processes are sluggish owing to the multistep proton-coupled electron-transfer processes (4e reactions) and complex reaction pathways, unavoidably leading to low efficiency and high overpotentials [4,5]. Therefore, the development of high-efficient and cost-effective bifunctional electrocatalyst for ORR and OER are key priorities [6–8]. Pt and its alloys have currently been considered as state-of-the-art ORR catalysts [9], while Ir and Ru have been regarded as the most active OER catalysts [10]. These catalysts have exhibited only single excellent catalytic activity, far away from the bifunctional oxygen electrocatalysts. Although two precious metals based

composites, such as Pt and Ir or Ru, have displayed moderate ORR and OER activities, their high cost and scarcity pose critical challenges for their practical application in energy systems [11–13]. It is thus imperative to develop the inexpensive bifunctional oxygen catalysts with robust efficiency for the widespread applications.

Doping of nitrogen in carbon materials can improve the catalytic activity owing to the enhanced electron-donor property and the formation of nitrogen-containing active sites. Consequently, nitrogen-doped carbon materials have drawn much attention because of their excellent catalytic performance toward both ORR and OER, low costing, and improved stability [14,15]. Especially, N-doped graphene (GR) or reduced graphene oxide (rGO) have been intensively explored to facilitate ORR and/or OER owing to its large surface area, superior conductivity, and excellent stability [16,17]. Nevertheless, GR sheets are tend to irreversibly form agglomerates or to restack due to the van der Waals force and π - π interactions [18]. This process can largely impair the catalytic efficiency of catalyst by decreasing the surface area, hindering the permeation of electrolytes, and reducing the accessible catalytic sites for O₂ and ions. Moreover, metal-free N-doped carbon materials showed the outstanding ORR activity with poor OER one. It is thus crucial to

* Corresponding authors.

E-mail addresses: trzhan@sdu.edu.cn (T. Zhan), wghou@sdu.edu.cn (W. Hou).

prevent GR sheets from aggregation and to incorporate metal ions in GR-based materials for an effective bifunctional oxygen catalyst.

The first-row transition-metal-based materials, especially Ni- and Fe-containing OER catalysts, are versatile substitutes for precious metal species due to their earth-abundance, low-costing, environmental benignity, and theoretically high catalytic activity. Recently, NiO, Ni(OH)₂, NiOOH [19–21], Ni-containing mixed-metal oxides (hydroxides) [19,20], and Ni-containing perovskites [22] have attracted much attention because of their high OER activity. Additionally, studies have demonstrated that combining Ni-based catalysts with iron (Fe) can further enhance their OER activities. Hence, various NiFe-based materials, including NiFe layered double hydroxides (LDH), NiFe/C, NiFe-LDH/rGO, FeNi-LDH/GR and NiFe-LDH/CNT have been extensively investigated as OER electrocatalysts [23–27]. Among them, LDH stands for a class of lamellar compounds with a generic chemical formula of [M_{1-x}^{II}M_x^{III}(OH)₂]^{x+}[(Aⁿ⁻)_{x/n}·mH₂O]. LDH consists of positively charged brucite-like layers and charge-balancing interlayer anions. The layered structure and water molecules endow it intrinsic catalytic and bulk redox activity [28]. Therefore, NiFe-LDH and its various composites have been found to be the efficient OER catalysts. Unfortunately, poor conductivities of the single LDH catalysts have severely limited their ORR catalytic activities. Thus, carbon materials such as GR, rGO and CNT are usually employed to improve the bifunctional catalytic ability.

Inspired by the high electro-active nature of Ni and Fe elements and the large surface area and excellent conductivity of rGO, it is believed that the porous composite of NiFe-LDH and N-doped rGO (NiFe-LDH/NrGO) can be an efficient bifunctional electrocatalyst of ORR and OER. Herein, the porous NiFe-LDH/NrGO nanospheres were synthesized through a one-pot solvothermal method in presence of surfactant. Wherein, the intimate hybridization of NiFe-LDH with rGO and N-doping can result in the enhanced conductivity, catalytic activity and stability. The NiFe-LDH/NrGO composite consequently showed the desirable catalytic performance toward both ORR and OER in alkaline medium, which could be attributed to the better synergistic effects of rGO, NiFe-LDH and doped nitrogen in the electrocatalyst.

2. Experimental

2.1. Chemicals

Graphite powder (average particle size 30 μm) was purchased from Colloid Chemical Co. (Shanghai, China). Melamine, ethylene glycol (EG) and sodium dodecyl sulfonate (SDS) were supplied by Aladdin Chemistry Co. (Shanghai, China) as analytical pure. Nafion solution (5%) was provided by DuPont Co. (USA). Polytetrafluoroethylene (PTFE: 60%, 0.20 μm) was obtained from Shenzhen Dechengwang S&T Ltd. All of the reagents were used as received without further purification.

2.2. Preparation of catalyst

2.2.1. Preparation of protonated g-C₃N₄ nanosheets

Protonated g-C₃N₄ nanosheets (p-CNNS) were prepared according to literature [29]. 5 g melamine was heated to 550 °C by a rate of 2.3 °C/min during 4 h and then calcined for additional 4 h in air at this temperature. The resultant yellow C₃N₄ was grinded to power in agate mortar. 0.5 g yellow powder was dissolved in 14 mL concentrated H₂SO₄ and stirred for 4 h at room temperature. The mixture was centrifugally washed with water until neutral condition and dried at 105 °C in air overnight. The corresponding protonated g-C₃N₄ (g-C₃N₄⁺) powder were further exfoliated in the concentrated HNO₃. The dispersion was stirred for 2 h and fur-

ther heated to 80 °C followed by consecutive ultrasonication for 4 h. Then the suspension was centrifugally washed with water to reached pH 7.0 and dried 60 °C in vacuum. As a result, the p-CNNS were afforded.

2.2.2. Preparation of NiFe-LDH/NrGO

GO was firstly prepared from nature graphite powder according to a modified Hummer's method [30]. Then the GO powder was re-dispersed in EG with its concentration as 1.0 wt%. NiFe-LDH/NrGO catalyst was synthesized by using a solvothermal method. Briefly, 0.1 g p-CNNS and mixed salts of NiCl₂·6H₂O (4.00 mmol) and FeCl₃·6H₂O (1.33 mmol) were added to 40 mL above EG solution (containing 1.0 wt% GO). Additionally, 0.6 g SDS was added and stirred for 2 h at 40 °C. The mixtures were transferred to the Teflon lined stainless steel reactor and solvothermal reacted at 180 °C for 36 h. By centrifuging and washing with water and ethanol orderly, the black NiFe-LDH/NrGO powders were prepared. By the similar method, the pure FeNi-LDH and NiFe-LDH/rGO products were also obtained for comparison in absence of p-CNNS or/and GO.

2.3. Characterization of catalyst

FT-IR spectra were recorded on a Nicolet iS10 spectrometer (ThermoFisher corporation). X-ray diffraction patterns (XRD) were performed on a Rigaku powder diffractometer equipped with Ni-filters Cu Kα radiation (λ = 1.54050 Å, 40 kV and 100 mA). The morphology was characterized by a JSM-6700F scanning electron microscope (SEM) and a JEOL JEM-2000EX transmission electron microscope (TEM) (Japan Electron Co.). By the BET method, the specific surface areas are calculated from N₂ adsorption isotherms by using an apparatus (Quantachrome-Autosorb-1C; Quantachrome Instr., USA). XPS was conducted on an HP 5950A ESCA spectrometer with an MgKα source.

2.4. Electrochemical measurements

Electrochemical measurements were conducted on a CHI 660D workstation with a standard three-electrode cell. The saturated Ag/AgCl and platinum flake (1 × 2 cm²) were respectively used as reference electrode and counter electrode. 0.1 M KOH solutions were respectively acted as electrolyte for ORR and OER. The reference potential was calibrated with respect to reversible hydrogen electrode (RHE) on the basis of the Nernst equation [31]:

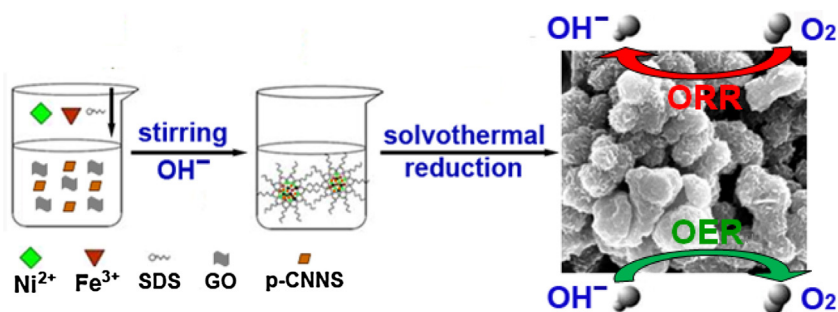
$$E_{\text{RHE}} = E_{\text{Ag/AgCl}} + 0.059\text{pH} + 0.1976 \quad (1)$$

ORR test: 10 mg of corresponding catalyst was dispersed in 500 μL Nafion ethanol solution (0.20 wt%) to form a homogeneous ink. Then 3 μL slurry was uniformly dropped on Rotating disk electrode (RDE, 0.196 cm²) and dried by blowing N₂. The final loading was 0.31 mg/cm². The electrolyte solution was saturated with N₂ or O₂ before each test. CV and LSVs was performed at a scan rate of 10 mV s⁻¹, LSVs was also recorded at 10 mV s⁻¹ with various rotate speeds (400–2025 rpm). The kinetic current density (*J_k*) was estimated according to the Koutecky–Levich (K-L) equation [8]:

$$\frac{1}{J} = \frac{1}{J_k} + \frac{1}{J_L} = \frac{1}{J_k} + \frac{1}{B \cdot \omega^{1/2}} \quad (2)$$

$$B = 0.62 \cdot n \cdot F \cdot C_0 \cdot D_0^{2/3} \cdot \nu^{1/6} \quad (3)$$

where *J* is the measured current density, *J_k* is the kinetic current density, *ω* is the electrode rotate speed, *n* represents the number of electron transferred per oxygen molecule, *F* is the Faraday constant (96485C/mol), *D₀* is the diffusion coefficient of O₂ in 0.1 M KOH (1.90 × 10⁻⁵ cm²/s), *ν* is the kinematic viscosity of the electrolyte (0.01 cm²/s), and *C₀* is the bulk concentration of O₂



Scheme 1. Schematic illustration for the synthesis of the NiFe-LDH/NrGO catalyst.

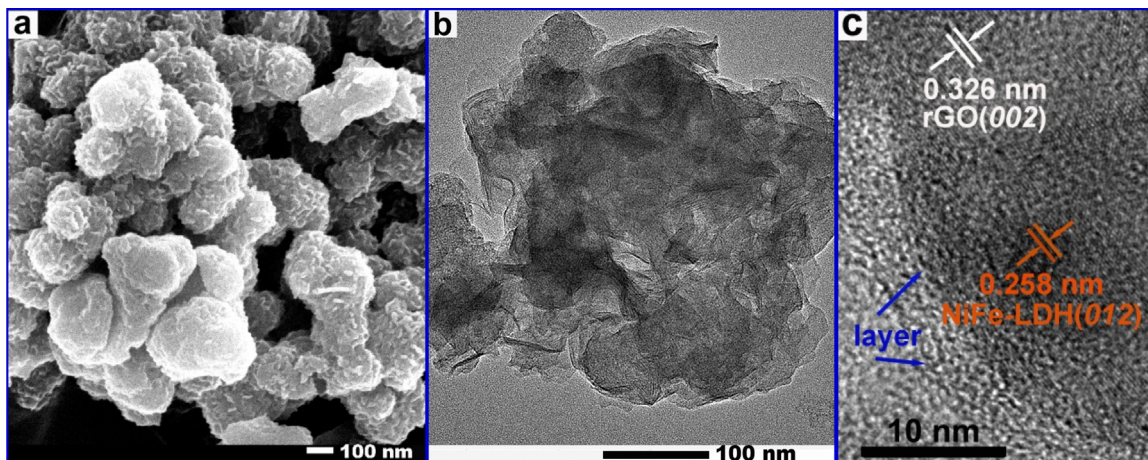


Fig. 1. SEM (a), TEM (b) and HRTEM (c) images of the as-prepared NiFe-LDH/NrGO composite.

($1.2 \times 10^{-6} \text{ mol/cm}^3$) [8]. The constant 0.2 is used when the rotate speed is expressed in rpm.

Rotating ring disk electrode (RRDE) measurements were performed on a glassy carbon disk with a polycrystalline Pt ring biased at 0.5 V (vs Ag/AgCl) at a rotating speed of 1600 rpm. The $\% \text{HO}_2^-$ and electron transfer number (n) were determined by the following equations [32]:

$$\% \text{HO}_2^- = \frac{200 \cdot I_d}{N \cdot I_d + I_r} \quad (4)$$

$$n = 4I_d / \left(I_d + \frac{I_r}{N} \right) \quad (5)$$

where I_d is the current of disk, I_r is the current of ring, and N is the current collection efficiency of the Pt ring. N was determined to be 0.40 from the reduction of $\text{K}_3\text{Fe}(\text{CN})_6$, well consisting with the manufacturer's value.

The chronoamperometric response for ORR was determined at -0.3 V (vs Ag/AgCl) of in O_2 -saturated 0.1 M KOH solution at 1600 rpm.

OER test: 10 mg of resulting catalyst was added in 400 μL ethanol containing 20 μL PTFE to form a homogeneous ink. Then 15 μL ink was dropped on a $1 \times 1 \text{ cm}^2$ Ni foam electrode (0.25 mm thickness) with the final loading of 0.36 mg/cm^2 . Linear sweep voltammetry (LSV) was carried out at a scan rate of 10 mV s^{-1} and the Tafel plots were transformed from LSV.

3. Results and discussion

3.1. Structural characterization of catalyst

Scheme 1 displays the systematic route to the preparation of the NiFe-LDH/NrGO electrocatalyst. Prior to preparation, the p-CNNS

was synthesized by protonation and exfoliation for the sake of the convenient doping of N species. As for the reaction mechanism, the hydrosoluble p-CNNS and hydrophilic GO nanosheets entered inside of SDS reverse micelles. And the mixed metal ions were also entrapped into the hydrophilic zone of micelles and anchored on the surface of GO and p-CNNS through electrostatic and complexing interactions. After introduction of alkaline, LDH crystallite gradually *in situ* formed in micelle inside. Finally, solvothermal reaction led to the crystallization of LDH nanoparticles accompanying the reduction of GO to rGO. Due to the effects of micelle and *in situ* growth of LDH, the porous NiFe-LDH/NrGO hierarchical nanospheres were gotten. The hierarchical nanostructure was also confirmed by the SEM image (Fig. 1a). It was distinct that NiFe-LDH occurred as thin nanosheets with lateral size about 30–80 nm and thickness less than 10 nm. These flakes combined the broken GO and p-CNNS nanoplatelets and built up the nanospheres with diameter *ca.* 100–300 nm. The formation of the hierarchical nanostructure could be mainly ascribed to the effects of reverse micelles. It was also observed the rough NiFe-LDH surface, manifesting the GO and p-CNNS nanosheets were anchored on LDH matrixes via electrostatic and non-covalent interactions. These phenomena were also verified by its TEM image (Fig. 1b). In the spherical nanostructure, the rGO and p-CNNS nanoparticles were intimately fused with the ultrathin NiFe-LDH nanosheets due to the electrostatic and complexing attractions of GO and p-CNNS toward the metal ions. During the solvothermal process, these lamellar building blocks ultimately gave rise to the porous NiFe-LDH/NrGO nanospheres owing to the confined roles of micelles. The interactions among three components were further evidenced by the corresponding HRTEM image. As shown in Fig. 1c, the composite mainly exhibited the almost semitransparent laminar morphology. There were clear layers like rGO or p-CNNS sheets occurred in the image. The

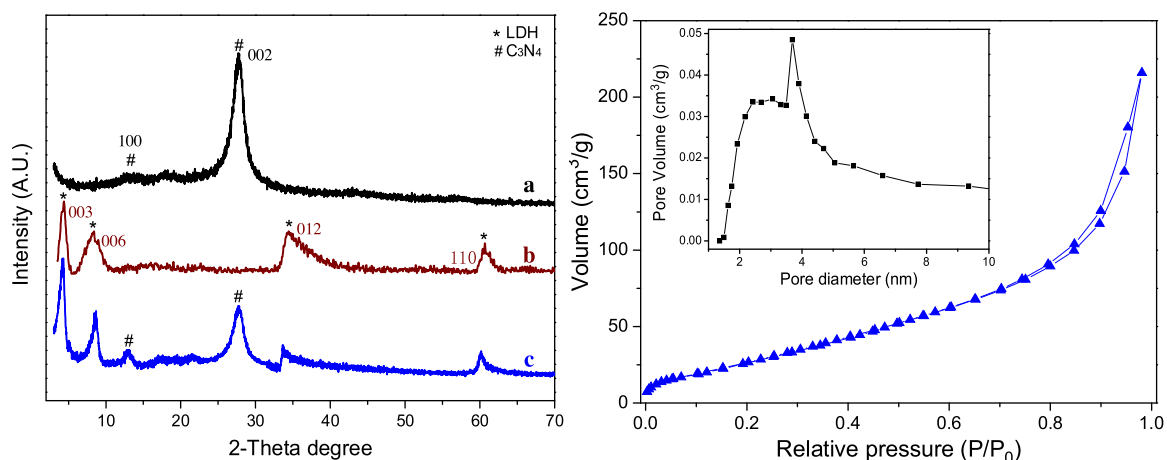


Fig. 2. (A) The XRD patterns of g-CNNS (a), NiFe-LDH/rGO (b) and NiFe-LDH/NrGO (c) composites. (B) BET and pore size distribution (inset) curves of NiFe-LDH/NrGO hybrid catalyst.

distinct lattice fringes showed the interplanar spacing values of 0.258 and 0.326 nm, respectively corresponding to $d_{(012)}$ of NiFe-LDH and $d_{(002)}$ of rGO (or p-CNNS). It was obvious that there was no apparent interface between the ultrathin rGO and p-CNNS due to the intimate and strong hybridization.

The XRD patterns of p-CNNS, NiFe-LDH/rGO and NiFe-LDH/NrGO hybrids were depicted in Fig. 2a. For the protonated nanosheets (curve a), p-CNNS still contained the strong (002) inter-

layer stacking peak at 27.8° arising from the conjugated aromatic system. However, only a weak (100) peak of in-planar repeating unit was observed at 13° . The results suggested that protonation decreased the crystalline and the orderliness of the planar structure of g-C₃N₄, but did not lose the graphite-like structure [29]. As regards NiFe-LDH/rGO composite (curve b), the LDH phase clearly showed the characteristic (003) (006), (012) and (110) peaks, indicating reservation of the hydroxalite structure. However, the (003)

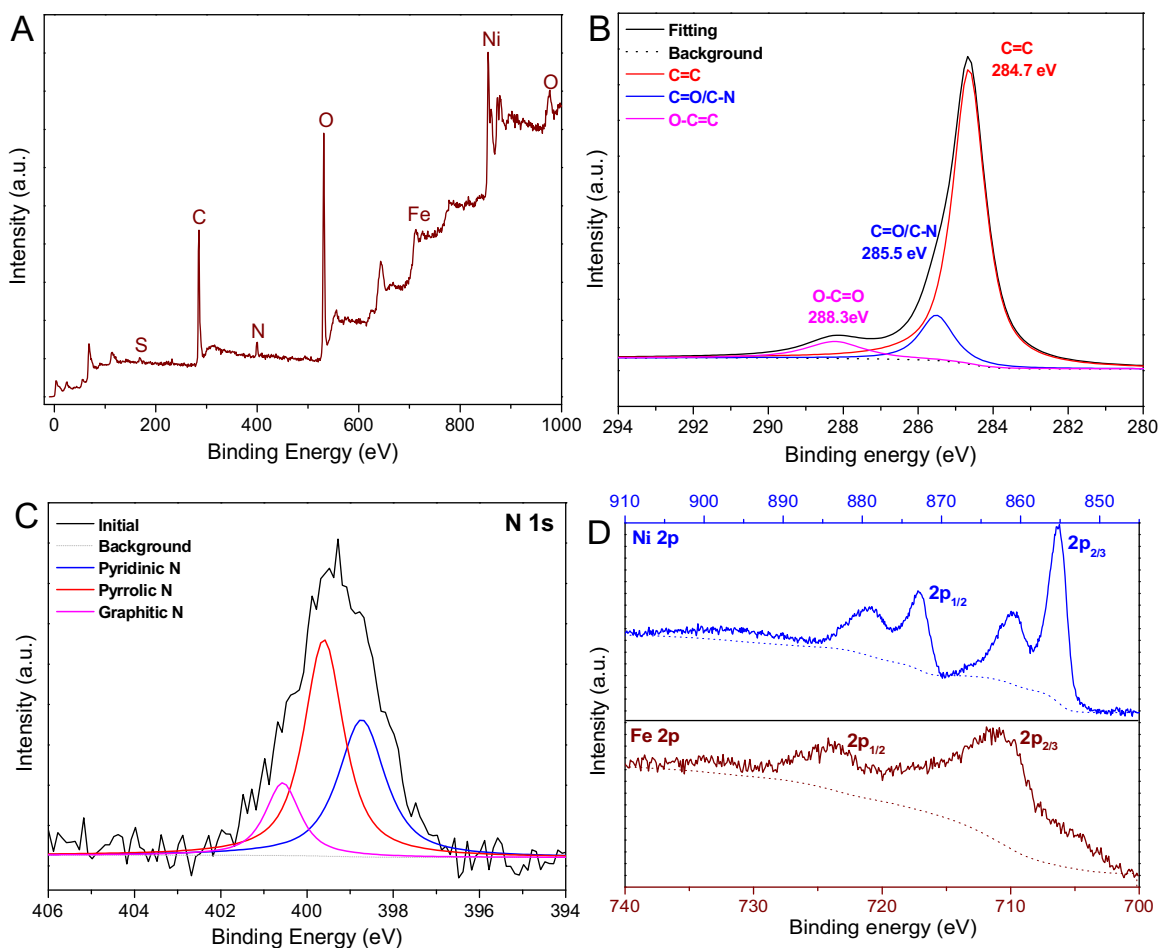


Fig. 3. XPS spectra of NiFe-LDH/NrGO composites survey (A); High resolution XPS spectra of C 1s (B) and N 1s (C) in NiFe-LDH/NrGO XPS; and XPS core level spectra of Ni-2p and Fe-2p (D).

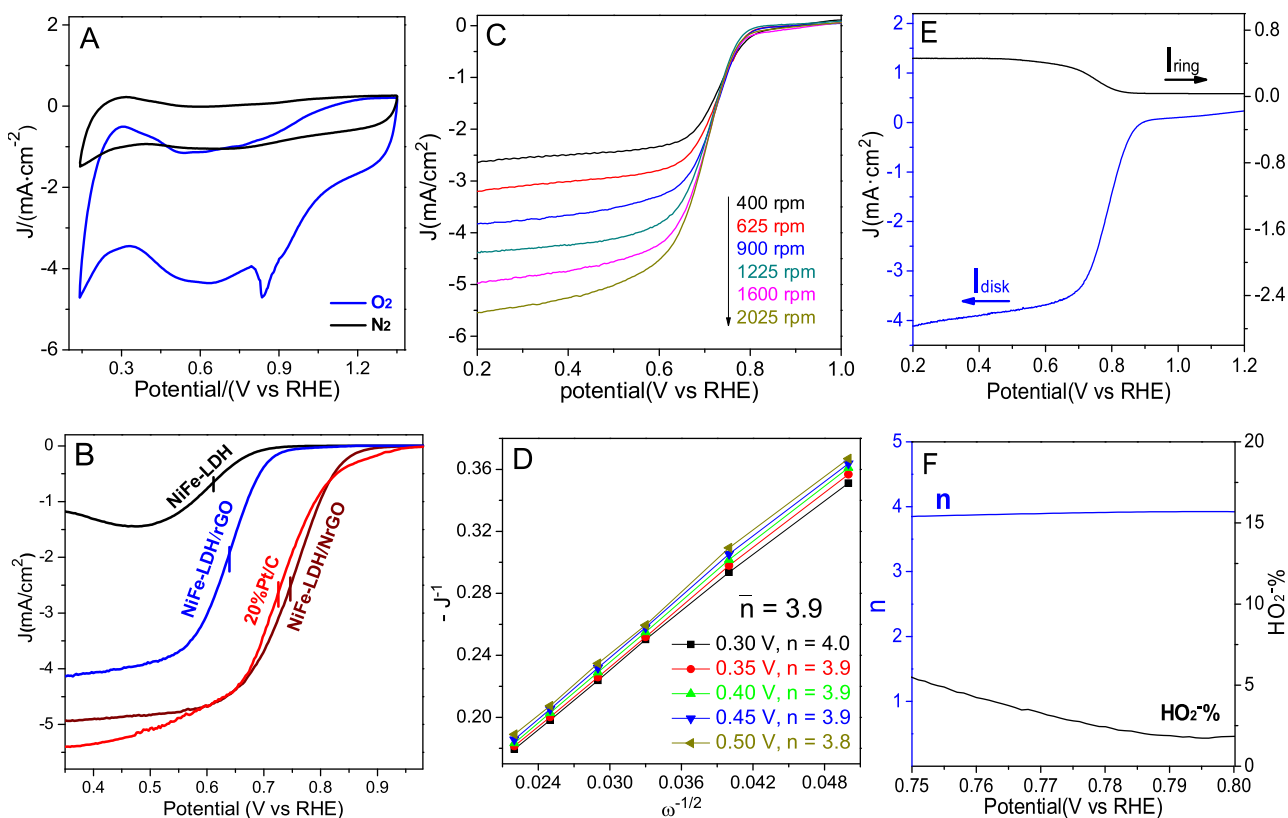


Fig. 4. (A) CVs in N_2 - and O_2 -saturated for NiFe-LDH/NrGO and (B) LSV in O_2 -saturated 0.1 M KOH for NiFe-LDH, NiFe-LDH/rGO, NiFe-LDH/NrGO and 20% Pt/C catalysts at 1600 rpm. (C) RDE voltammograms of NiFe-LDH/NrGO in O_2 -saturated 0.1 M KOH at a scan rate of 10 mV s^{-1} at different rotating speed and (D) the corresponding K-L plot of j^{-1} vs. $\omega^{-1/2}$. The inset shows the electron transfer number (n). (E) RRDE voltammograms of NiFe-LDH/NrGO in O_2 -saturated 0.1 M KOH. The disk potential is scanned at 10 mV s^{-1} and the ring potential is constant at 1.3 V. (F) The electron transfer number n and percentage of HO_2^- at certain potentials based on the corresponding RRDE results.

and (006) peaks clearly moved to the lower degree compared to those for pristine LDH, ascribing to the intercalation of SDS and GO components [23]. The larger d_{003} value (2.385 nm) could further evidence it. After doping p-CNNS, NiFe-LDH/NrGO exhibited the characteristic reflections of both NiFe-LDH and p-CNNS (curve c). It should be noted that the rGO reflections were barely found in both NiFe-LDH/rGO and NiFe-LDH/NrGO products, revealing that the strong interactions and intimate hybridization of rGO with LDH (and p-CNNS) nanosheets facilitated the former well dispersed [33].

The chemical structure of electrocatalysts was further confirmed by FT-IR spectroscopy. As shown in Fig. S1, pristine p-CNNS (black curve) displayed the typical adsorption peaks of $g\text{-C}_3\text{N}_4$ nanosheets at around 810 cm^{-1} for heptazine ring system, $900\text{--}1800 \text{ cm}^{-1}$ for s-triazine derivatives, and $3000\text{--}3550 \text{ cm}^{-1}$ for the N–H stretching [34]. As for NiFe-LDH/rGO (brown curve), there mainly appeared the characteristic peaks of hydrotalcite at about $550\text{--}620 \text{ cm}^{-1}$ (ν_{MO}), 430 cm^{-1} (ν_{OMO}) and the adsorption bands of SDS at 1047 and 1188 cm^{-1} for the S=O stretches, 1464 and $2830\text{--}2970 \text{ cm}^{-1}$ for the C–H stretches [35]. In the case of the NiFe-LDH/NrGO composite (blue curve), the classical adsorption bands of p-CNNS and NiFe-LDH/rGO could be easily seen. However, the peak shape and intensity experienced some extent change owing to the strong interactions between components. The results highly indicated that p-CNNS was successfully doped in the composite.

The N_2 adsorption-desorption isotherms were employed to determine the surface area and porous nanostructure of NiFe-LDH/NrGO. As illustrated in Fig. 2B, the isotherm curve presented a typical IV profile with a classical H3-type hysteresis loop, revealing the well-developed slit-type pore system corresponding to the general nanosheet-like microstructure [36]. The BET surface area was obtained as $130.94 \text{ m}^2/\text{g}$ according to the N_2 adsorption isotherm,

which was higher than those for the previously reported LDH [37]. The mesopore size distribution plot (Fig. 2B inset) showed a narrow peak about 2–6 nm, might consist with the abundant tiny pores in NiFe-LDH/NrGO nanospheres. It could be supposed that both the higher specific surface area and the unique 3D porous nanosphere could endow NiFe-LDH/NrGO with an excellent catalytic activity due to the higher active site density and the lower mass transport resistance [8].

The elemental composition of the NiFe-LDH/NrGO catalyst was also investigated by XPS. As shown in Fig. 3A, the XPS survey spectrum exhibited a sharp C 1s peak at 285.1 eV, a N 1s peak at 400.1 eV, an O 1s peak at 531.1 eV, a Ni 2p peak at 856.1 eV, and a Fe 2p peak at 713.1 eV, highly proving the successful preparation of the NiFe-LDH/NrGO composite. The contents of C, O, N, Fe and Ni were analyzed to be 55.02, 29.41, 7.00, 2.20 and 6.38 at.%, respectively. The high-resolution C 1s XPS spectra showed three different functional carbon species including a C=C bond at 284.7 eV, a C=O/C–N bond at 285.5 eV, and a O–C–O bond at 288.3 eV (Fig. 3B) [38]. The predominant non-oxygenated C specie (C=C) indicated that the GO component was successfully transformed into rGO after heating treatment. It could be seen that the high-resolution N 1s XPS spectra (Fig. 3C) revealed three types of nitrogen species including pyridinic N, pyrrolic N and graphitic N at 398.7, 399.6 and 400.6 eV, which are consistent with the pristine p-CNNS (Fig. S2) and other assignments in literature [32]. However, the content of the pyrrolic N clearly increased from 32.75% to 51.57% compared to p-CNNS, but those for pyridinic N and graphitic N decreased from 43.90% and 23.35% to 35.10% and 13.33%, respectively. The change of the concentrations of N species in NiFe-LDH/NrGO was predominantly attributed to the hydrothermal treatment. Anyway, in the composited catalyst pyridinic-N and graphitic-N were the

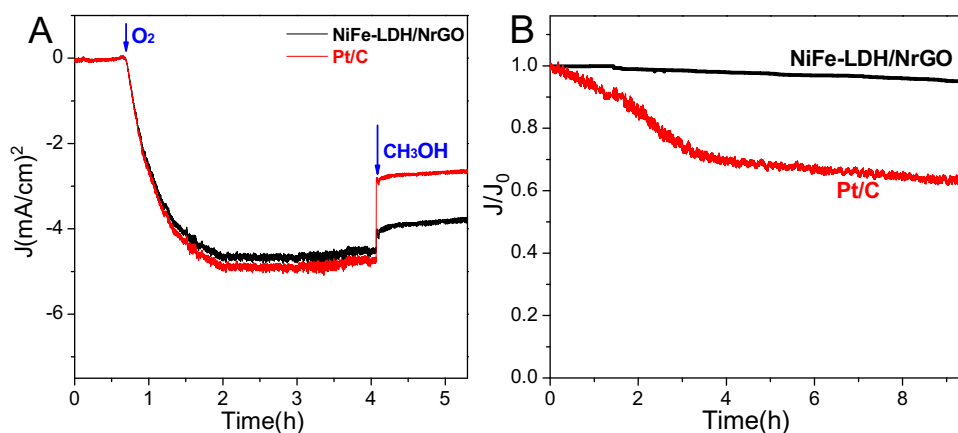


Fig. 5. (A) Current–time chronoamperometric responses of NiFe-LDH/rGO and 20%Pt/C at 0.5 V (vs RHE) in 0.1 M KOH. The arrows indicate the addition of O_2 and methanol. (B) Current-time responses of NiFe-LDH/NrGO and 20%Pt/C at a rotating rate of 1600 rpm in O_2 saturated 0.1 M KOH.

dominant species. It is well known that the pyridinic-N and pyrrolic-N are generally considered as efficient ORR active sites, in which the former can enhance the onset potential for ORR, whereas the latter can improve the limiting current density [39]. In the Ni 2p spectra (Fig. 3D up), the two distinct peaks centered at 855.4 and 872.3 eV corresponding to the satellite signals of Ni 2p_{3/2} and Ni 2p_{1/2}, respectively [40]. The results showed the presence of Ni²⁺ species in the catalyst. The Fe 2p spectra (Fig. 3D down) displayed the Fe 2p_{3/2} and Fe 2p_{1/2} peaks at 712.3 and 725.8 eV, demonstrating the +3 oxidation state in the composite [41].

3.2. Electrochemical ORR and OER activities

The electrocatalytic performance toward ORR of the catalyst was examined in 0.1 M KOH solution with a typical three-electrode cell. In order to assess the ORR activity, the comparative CVs both in O_2 - and N_2 -saturated 0.1 M NaOH aqueous solution were recorded at scan rate of 10 mV s⁻¹ as illustrated in Fig. 4A. The NiFe-LDH/NrGO catalyst displayed a featureless CV curve in N_2 -saturated electrolyte during the chosen potential range. After being saturated with O_2 , the prominent cathodic peak appeared at +0.836 V, suggesting an excellent ORR catalytic activity for NiFe-LDH/NrGO in alkaline media. To further investigate the roles the doped nitrogen on ORR, the LSVs of NiFe-LDH, NiFe-LDH/rGO, NiFe-LDH/NrGO and 20% Pt/C catalysts were performed as presented in Fig. 4B. The NiFe-LDH/NrGO composite exhibited the superior ORR activity to NiFe-LDH and NiFe-LDH/rGO. The onset potential and half-wave potential of NiFe-LDH/NrGO were 0.91 V and 0.75 V, respectively, which are close to the activity of commercial 20% Pt/C catalyst (0.94 V and 0.73 V) and largely more positive than those for NiFe-LDH (0.75 V and 0.61 V) and NiFe-LDH/rGO (0.79 V and 0.64 V) counterparts. Moreover, its diffusion-limiting current density value (at 0.5 V) is slightly lower than that for Pt/C and much higher than those for NiFe-LDH and NiFe-LDH/rGO catalysts. The results divulged that the doping of p-CNNS greatly facilitated the intrinsic catalytic activity and effectively decreased mass transport resistance between reactants and catalysts [42]. For the sake of the ORR kinetics, a series of polarization curves of NiFe-LDH/NrGO (Fig. 4C) and NiFe-LDH/rGO (Fig. S3A) were also determined by RDE at different rotating speeds between 400 to 2025 rpm. The limiting current density of both catalysts increased with increasing rotating speed because of the gradually shortened diffusion distance [39]. The corresponding K-L plots ($-j^{-1}$ vs. $\omega^{-1/2}$) were obtained from the LSV diffusion limiting current densities at various potentials as shown in Fig. 4D and Fig. S3B, respectively. The transferred electrons numbers (n) of NiFe-LDH/rGO and NiFe-LDH/NrGO were calculated to

be 3.7 and 3.9, respectively. Although these values demonstrated that both ORR processes were predominated by a 4-electron transfer pathway, the n values of 3.9 manifested that the NiFe-LDH/NrGO catalyst could directly reduce oxygen to water. As a result, the doping N resulted in the more efficient ORR catalytic performance compared to NiFe-LDH/rGO. This was confirmed again by their RRDE tests as shown in Figs. 4E and S3C. The ring current of NiFe-LDH/NrGO was much lower than that of NiFe-LDH/rGO, revealing that the oxidation of peroxide generated on the former catalyst was suppressed to a greater degree than the latter [39]. The n values and the HO_2^- yields were accurately estimated according to above ring and disk current and the results were presented in Figs. 4F and S3D. It was obvious that the n value for NiFe-LDH/NrGO was higher than that for NiFe-LDH/rGO, highly consistent with their K-L results. The HO_2^- yields on NiFe-LDH/NrGO was less than 5% in a wide potential window, whereas the average HO_2^- yield for NiFe-LDH/rGO was only below 10%. It was supposed that the porous nanostructure cross-linked by packed nanosheets provided abundant active sites and convenient mass-transfer channels, leading to an excellent ORR activity.

For the practical applications in fuel cell, the tolerance to methanol crossover is a challenging issue for ORR catalysts and also a short slab of precious metal-based catalysts. The methanol crossover effect of NiFe-LDH/NrGO catalyst was determined at 0.50 V with a rotating rate of 1600 rpm, because the current density was the highest and the most stable under this condition [43]. The chronoamperometric responses of NiFe-LDH/NrGO and 20%Pt/C were given in Fig. 5A. At beginning, the introduction of O_2 induced the conspicuous increasing of the ORR current on both catalysts, indexing their good ORR activity. After adding methanol to alkali solution (reaching 1 M), the currents of Pt/C catalyst instantaneously decreased owing to mixing the oxidation current of methanol. Nevertheless, the NiFe-LDH/NrGO hybrid displayed the nearly unchangeable current response, suggesting its superior tolerance ability against methanol crossover. Long-term stability is also of importance for commercial catalysts. Herein, chronoamperometric measurements were performed to comparatively evaluate the durability of NiFe-LDH/NrGO and Pt/C catalysts under the same conditions (Fig. 5B). After continuous testing for 9.5 h, NiFe-LDH/NrGO experienced the slight performance attenuation by 4.9%, whereas Pt/C catalyst underwent a large current reduction by 36.8%. Generally, Pt component in commercial Pt/C catalyst is easily dissolved and sintered under working conditions and the carbon black constituent are poorly stable, thus leading to the surface particles dissolution/aggregation. These results highly suggested that NiFe-LDH/NrGO possessed a better methanol tolerance ability and

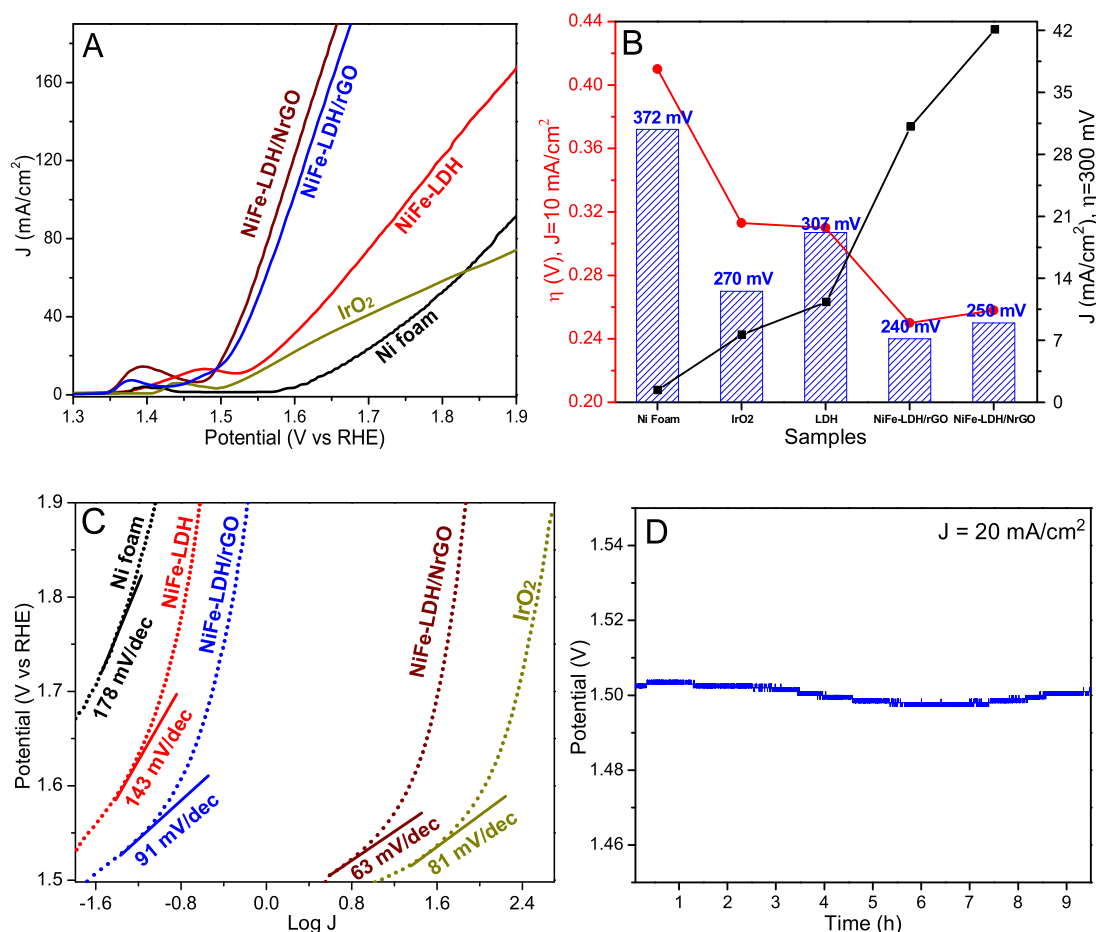


Fig. 6. (A) LSVs for OER on different modified electrode. (B) Onset overpotentials of different modified electrode (column); Overpotentials of different modified electrode at $J = 10$ mA cm⁻² (circle symbol); Current densities at $\eta = 300$ mV of different modified electrode (square symbol). (C) Tafel plots derived from the corresponding LSVs. (D) Chronopotentiometry curve of NiFe-LDH/NrGO catalyst. (For interpretation of the references to colour in this figure legend, the reader is referred to the web version of this article.)

endurable stability by comparison with commercial 20%Pt/C catalyst. The excellent ORR activity of NiFe-LDH/NrGO could be attributable to the stable structure of the heteroatom-doped carbon material [43].

Considering the potential bifunctional activities, the OER performance was also assessed in 0.1 M KOH by coating different catalysts on Ni foam as working electrode. Firstly, the OER polarization curves for Ni foam, IrO₂, NiFe-LDH, NiFe-LDH/rGO and NiFe-LDH/NrGO were determined as shown in Fig. 6A and their related parameters were illustrated in Fig. 6B. Noticeably, bare Ni foam exhibits the very poor OER activity accompanying a distinct oxidation peak of Ni at 1.39 V. The LSV of NiFe-LDH/rGO exhibited a more negative onset overpotential (240 mV) and a far larger current density than pristine NiFe-LDH (onset overpotential: 307 mV), revealing the former's outstanding OER activity due to incorporating rGO component. After doping N, although NiFe-LDH/NrGO displayed a slightly more positive onset overpotential (258 mV) than the non-doped counterpart (240 mV for NiFe-LDH/rGO), this value was much lower than Ni foam (372 mV), IrO₂ (270 mV) and the previous report for IrO₂ (290 mV) [24] and those of ZnCo- (340 mV) [44], CoFe- (397 mV) [45], CoNi- (393 mV) [46] and NiCo-LDH (290 mV) [40], and even compare to that of the best reported NiFe-LDH/CNT (220 mV) [27]. Moreover, the NiFe-LDH/NrGO porous nanospheres showed an overpotential of 258 mV at 10 mA cm⁻², indexing approximately the current density for a 10% efficient solar-to-fuel conversion device [10]. This value was

much lower than those of Ni foam (410 mV), IrO₂ (313 mV) and pristine NiFe-LDH (310 mV), but slightly larger than that of NiFe-LDH/rGO catalyst (250 mV). At this stage, it seemed that the doping N atom slightly impaired the OER activity of NiFe-LDH/NrGO. On the other hand, the current density at an overpotential (η) of 300 mV is also important for quantification of OER activity. The current density of the NiFe-LDH/NrGO composite reached 42.12 mA cm⁻² at $\eta = 300$ mV, which was far higher than those for Ni foam (1.37 mA cm⁻²), IrO₂ (7.64 mA cm⁻²), pristine NiFe-LDH (11.34 mA cm⁻²) and NiFe-LDH/rGO (31.15 mA cm⁻²). Fig. 6C displayed the tafel curves of three catalysts. The NiFe-LDH/NrGO nanohybrid performed the lowest tafel slope of 63 mV dec⁻¹ compared with Ni foam (178 mV dec⁻¹), IrO₂ (81 mV dec⁻¹), NiFe-LDH (143 mV dec⁻¹) and NiFe-LDH/rGO (91 mV dec⁻¹). The higher current density at $\eta = 300$ mV and the smaller tafel slope manifested that the porous NiFe-LDH/NrGO composite showed the remarkable OER kinetics at $\eta > 300$ mV due to a more facile charge transfer through the porous NiFe-LDH/NrGO nanochannels. The durability of NiFe-LDH/NrGO toward OER was determined in 0.1 M KOH by the chronopotentiometry at a constant current density of 20 mA cm⁻² (Fig. 6D). About 2 mV loss of potential after 9.5 h implied the outstanding durability of the NiFe-LDH/NrGO catalyst for OER. Overall, the N doping by using p-CNNs was not as effective as that in the ORR process because of the different active species for ORR and OER [47] in the same catalyst.

4. Conclusion

Porous NiFe-LDH/NrGO nanospheres were prepared as a novel bifunctional oxygen catalyst through one pot method by using GO, p-CNNS, mixed metal salts and alkali as precursors. Compared to pristine NiFe-LDH and NiFe-LDH/rGO, NiFe-LDH/NrGO displayed better ORR activity in alkaline solution involving a perfect 4e pathway. Its methanol tolerance and durability ability for ORR were outperformed as well. The NiFe-LDH/NrGO hybrid exhibited a comparable OER activity to NiFe-LDH/rGO with close onset overpotentials but a lower overpotential and a larger current density at $\eta > 300$ mV. To best of our knowledge, it was the first time that NiFe-LDH/NrGO was studied as an efficient bicatalyst. The prominent performance of NiFe-LDH/NrGO was explained in three aspects, such as doping N atom and porous nanosphere structure as well as the strong coupling interactions among rGO, LDH and p-CNNS building blocks. These strategies provided abundant active sites and convenient mass-transfer channels for the improvement of the ORR and OER electrochemical performance.

Acknowledgements

This work is financially supported by the National Natural Science Foundation of China (21173135, 21403121, 21573133 and 21405088), the Natural Science Foundation of Shandong Province, China (ZR2014JL013 and ZR2013BQ013), the open foundation from the Key Laboratory of Marine Bioactive Substance and Modern Analysis Technology, SOA (MBSMAT-2016-02, MBSMAT-2015-04, MBSMAT-2014-02 and MBSMAT-2013-01).

Appendix A. Supplementary data

Supplementary data associated with this article can be found, in the online version, at <http://dx.doi.org/10.1016/j.apcatb.2017.01.010>.

References

- [1] I. Katsounaros, S. Cherevko, A.R. Zeradjanin, K.J. Mayrhofer, *Angew. Chem. Int. Ed.* 53 (2014) 102–121.
- [2] M.G. Walter, E.L. Warren, J.R. McKone, S.W. Boettcher, Q. Mi, E.A. Santori, N.S. Lewis, *Chem. Rev.* 110 (2010) 6446–6473.
- [3] H. Wang, H. Dai, *Chem. Soc. Rev.* 42 (2013) 3088–3113.
- [4] F. Jiao, H. Frei, *Angew. Chem. Int. Ed.* 48 (2009) 1841–1844.
- [5] Y. Liang, H. Wang, J. Zhou, Y. Li, J. Wang, T. Regier, H. Dai, *J. Am. Chem. Soc.* 134 (2012) 3517–3523.
- [6] S.L. Candelaria, Y. Shao, W. Zhou, X. Li, J. Xiao, J.G. Zhang, Y. Wang, J. Liu, J. Li, G. Cao, *Nano Energy* 1 (2012) 195–220.
- [7] S. Chen, J. Duan, M. Jaroniec, S.Z. Qiao, *Adv. Mater.* 26 (2014) 2925–2930.
- [8] T. Liu, Y.F. Guo, Y.M. Yan, F. Wang, C. Deng, D. Rooney, K.N. Sun, *Carbon* 106 (2016) 84–92.
- [9] V.R. Stamenkovic, B. Fowler, B.S. Mun, G. Wang, P.N. Ross, C.A. Lucas, N.M. Markovic, *Science* 315 (2007) 493–497.
- [10] C.C. Mccrory, S. Jung, J.C. Peters, T.F. Jaramillo, *J. Am. Chem. Soc.* 135 (2013) 16977–16987.
- [11] Y.C. Lu, Z. Xu, H.A. Gasteiger, S. Chen, K. Hamad-Schifferli, S.H. Yang, *J. Am. Chem. Soc.* 132 (2010) 12170–12171.
- [12] Z. Jian, P. Liu, F. Li, P. He, X. Guo, M. Chen, H. Zhou, *Angew. Chem. Int. Ed.* 53 (2014) 442–446.
- [13] F.D. Kong, S. Zhang, G.P. Yin, N. Zhang, Z.B. Wang, C.Y. Du, *J. Power Sources* 210 (2012) 321–326.
- [14] Z. Mo, R. Zheng, H. Peng, H. Liang, S. Liao, *J. Power Sources* 245 (2014) 801–807.
- [15] Y. Zhao, K. Kamiya, K. Hashimoto, S. Nakanishi, *J. Phys. Chem. C* 119 (2015) 2583–2588.
- [16] I.Y. Jeon, H.J. Choi, S.M. Jung, J.M. Seo, M.J. Kim, L. Dai, J.B. Baek, *J. Am. Chem. Soc.* 135 (2012) 1386–1393.
- [17] S. Chen, J. Duan, M. Jaroniec, S.Z. Qiao, *Angew. Chem. Int. Ed.* 52 (2013) 13567–13570.
- [18] Y. Li, W. Zhou, H. Wang, L. Xie, Y. Liang, F. Wei, J.C. Idrobo, S.J. Pennycook, H. Dai, *Nat. Nanotechnol.* 7 (2012) 394–400.
- [19] L. Trotochaud, J.K. Ranney, K.N. Williams, S.W. Boettcher, *J. Am. Chem. Soc.* 134 (2012) 17253–17261.
- [20] R.D. Smith, M.S. Prévot, R.D. Fagan, Z. Zhang, P.A. Sedach, M.K. Siu, S. Trudel, C.P. Berlinguette, *Science* 340 (2013) 60–63.
- [21] M. Gao, W. Sheng, Z. Zhuang, Q. Fang, S. Gu, J. Jiang, Y. Yan, *J. Am. Chem. Soc.* 136 (2014) 7077–7084.
- [22] J. Suntivich, S. Jin, K.J. May, H.A. Gasteiger, J.B. Goodenough, Y. Shao-horn, *Science* 334 (2012) 1383–1385.
- [23] X. Long, J. Li, S. Xiao, K. Yan, Z. Wang, H. Chen, S. Yang, *Angew. Chem. Int. Ed.* 53 (2014) 7584–7588.
- [24] D.H. Youn, Y.B. Park, J.Y. Kim, G. Magesh, Y.J. Jang, J.S. Lee, *J. Power Sources* 294 (2015) 437–443.
- [25] Y. Feng, H. Zhang, Y. Zhang, X. Li, Y. Wang, *ACS Appl. Mater. Interfaces* 7 (2015) 9203–9210.
- [26] O. Diazmorales, I. Ledezmayanez, M.T.M. Koper, F. Callevallejo, *ACS Catal.* 5 (2015) 2060–2086.
- [27] M. Gong, Y. Li, H. Wang, Y. Liang, J.Z. Wu, J. Zhou, J. Wang, T. Regier, F. Wei, H. Dai, *J. Am. Chem. Soc.* 135 (2013) 8452–8455.
- [28] F. Song, X. Hu, *Nat. Commun.* 5 (2014), 4477–4477.
- [29] Y.J. Zhang, A. Thomas, M. Antonietti, X. Wang, *J. Am. Chem. Soc.* 131 (2009) 50–51.
- [30] W.S. Hummers, R.E. Offeman, *J. Am. Chem. Soc.* 80 (1958), 1339–1339.
- [31] A. Ramírez, P. Hillebrand, D. Stellmach, M.M. May, P. Bogdanoff, S. Fiechter, *J. Phys. Chem. C* 118 (2014) 14073–14081.
- [32] X. Qiao, S. Liao, R. Zheng, Y. Deng, H. Song, L. Du, *ACS Sustain. Chem. Eng.* 4 (2016) 4131–4136.
- [33] T. Zhan, X. Wang, X. Li, Y. Song, W. Hou, *Sens. Actuators B Chem.* 228 (2016) 101–108.
- [34] P. Niu, L. Zhang, G. Liu, H. Cheng, *Adv. Funct. Mater.* 22 (2012) 4763–4770.
- [35] J. Zhao, X. Fu, S. Zhang, W. Hou, *Appl. Clay Sci.* 51 (2011) 460–466.
- [36] G.H. Dong, L.Z. Zhang, *J. Mater. Chem.* 22 (2011) 1160–1166.
- [37] T. Zhan, Y. Zhang, Q. Yang, H. Deng, J. Xu, W. Hou, *Chem. Eng. J.* 302 (2016) 459–465.
- [38] H. Li, G. Zhu, Z.H. Liu, Z. Yang, Z. Wang, *Carbon* 48 (2010) 4391–4396.
- [39] R. Li, Z. Wei, X. Gou, *ACS Catal.* 5 (2015) 4133–4142.
- [40] J. Jiang, A. Zhang, L. Li, L. Ai, *J. Power Sources* 278 (2015) 445–451.
- [41] L.J. Zhou, X. Huang, H. Chen, P. Jin, G.D. Li, X. Zou, *Dalton Trans.* 44 (2015) 11592–11600.
- [42] E. Bayram, G. Yilmaz, S. Mukerjee, *Appl. Catal. B Environ.* 192 (2016) 26–34.
- [43] Q. Liu, J. Jin, J. Zhang, *ACS Appl. Mater. Interfaces* 5 (2013) 5002–5008.
- [44] X. Zou, A. Goswami, T. Asefa, *J. Am. Chem. Soc.* 135 (2013) 17242–17245.
- [45] G. Abellan, J.A. Carrasco, E. Coronado, J. Romero, M. Varela, *J. Mater. Chem. C* 2 (2014) 3723–3731.
- [46] Y. Zhang, B. Cui, C. Zhao, H. Lin, J. Li, *Phys. Chem. Chem. Phys.* 15 (2013) 7363–7369.
- [47] Y. Gorlin, T.F. Jaramillo, *J. Am. Chem. Soc.* 132 (2010) 13612–13614.